Thermal Structure of the Martian Upper Mesosphere/Lower Thermosphere From MAVEN/IUVS Stellar Occultations

Sumedha Gupta, Roger V. Yelle, Nicholas M. Schneider, Sonal K. Jain, Francisco González-Galindo, Loïc Verdier, Ashwin Braude, Franck Montmessin, Majd Mayyasi, Justin Deighan, et al.

HAL Id: insu-03870947

https://insu.hal.science/insu-03870947

Submitted on 11 May 2023

Correspondence to:

S. Gupta,
sumedha.gupta@lasp.colorado.edu

Thermal Structure of the Martian Upper Mesosphere/Lower Thermosphere From MAVEN/IUVS Stellar Occultations

Sumedha Gupta[1], Roger V. Yelle[2], Nicholas M. Schneider[1], Sonal K. Jain[1], Francisco González-Galindo[3], Loic Verdier[4], Ashwin S. Braude[4], Franck Montmessin[4], Majd Mayyasi[5], Justin Deighan[1], and Shannon Curry[6]

[1]Laboratory for Atmospheric and Space Physics, University of Colorado Boulder, Boulder, CO, USA, [2]Lunar and Planetary Laboratory Science, University of Arizona, Tucson, AZ, USA, [3]Instituto de Astrofísica de Andalucía, CSIC, Granada, Spain, [4]Laboratoire Atmosphères, Milieux, Observations Spatiales, CNRS/UVSQ Université Paris-Saclay/UPMC, Guyancourt, France, [5]Center for Space Physics, Boston University, Boston, MA, USA, [6]Space Sciences Laboratory, University of California, Berkeley, Berkeley, CA, USA

Abstract We report the first detailed study of the diurnal thermal structure of upper mesosphere/lower thermosphere (~80 to 160 km) of Mars from stellar occultation observations by the Imaging Ultraviolet Spectrograph (IUVS) aboard the NASA Mars Atmosphere and Volatile EvolutioN (MAVEN) spacecraft. Due to stray light contamination, analyses of this data set to date have been confined to the nighttime events. This study makes use of a revised algorithm for removal of stray light from occultation spectra to retrieve the dayside events as well. The dayside is observed to be warmer than the nightside, with the maximum day/night difference of ~30 K in the lower thermosphere, ~20 K around the mesopause, with little diurnal variations at lower altitudes. This is consistent with the radiative time constant which is of the order of 1 Mars day in the 3×10^{-4} to 3×10^{-3} Pa region. The data also shows that the regions at pressure less than 2×10^{-3} Pa are under strong solar control with no prominent migrating tidal signatures. In contrast, on Earth, the radiative time constant near the mesopause is ~10 Earth days and the temperature variations due to tides are quite large. The Mars Climate Database shows a diurnal trend opposite to the data in the mesosphere, with the dayside mesopause predicted to be cooler than the nightside by ~10 K along with signatures of a vertically propagating tide. The IUVS data set provides an unprecedented constraint on the structure of the Martian mesosphere.

Plain Language Summary The dayside Mars Atmosphere and Volatile EvolutioN/Imaging Ultraviolet Spectrograph stellar occultation observations are often contaminated by stray light and are not processed by the current data reduction pipeline. We have developed an improved algorithm to retrieve these dayside events as well, therefore expanding the usable data set. There have been very few observations of Mars in 80–160 km altitude range, a region that is influenced by the wave perturbations from lower atmosphere and solar forcing from above, with no data set providing a complete local time coverage to study the day/night differences. Therefore, we have enabled the first detailed study of the diurnal thermal structure of Mars in this region by salvaging the dayside events. We find the dayside atmosphere to be always warmer than the nightside at these altitudes. Though it is expected but has not been established for the Martian mesosphere. In contrast, the Mars Climate Database shows an opposite diurnal trend at the mesopause, along with inconsistent tidal signatures with the data. The mesopause is controlled by the energy balance between radiative processes. These data-model inconsistencies thus imply that our current understanding of the dynamics and structure of the Martian mesosphere is inadequate and this data set can provide important constraints on the models.

1. Introduction

Recent Mars missions have provided a wealth of observations to study the red planet and its relationship to Earth. Nonetheless, there are still gaps in our understanding of the Martian upper mesosphere/lower thermosphere, a region that includes the mesopause (~100 km) and homopause (~125 km), and is closely coupled to the atmospheric layers above and below. The thermal structure of this altitude range (~80 to 160 km) is critical in understanding the coupling processes, global circulation patterns, energy balance, and atmospheric loss (Haberle et al., 2017).

There have been some previous observations of the upper mesosphere and lower thermosphere measurements above ~80 km with existing datasets providing only limited temporal (diurnal, seasonal, and inter-annual) and

spatial coverage. Temperature measurements for a limited altitude range of the mesosphere (∼90 to 105 km) and thermosphere (∼170 to 190 km) were examined by Jain et al. (2021) from limb observations by the Imaging Ultraviolet Spectrograph (IUVS) instrument aboard the Mars Atmosphere and Volatile EvolutioN (MAVEN) spacecraft. These temperatures were retrieved from the dayglow emissions and are therefore confined to the dayside (LT = 6–18). Day/night temperatures in the lower thermosphere are reported by Stone et al. (2018) from the Neutral Gas and Ion Mass Spectrometer aboard MAVEN down to ∼125 km, but these are from 8 deep-dip campaigns and therefore are limited to a small number of local times, latitudes, and Martian seasons. Thiemann et al. (2018) presented the density and temperature retrievals in 120–200 km altitude range from the Extreme Ultraviolet (EUV) Monitor (EUVM) on MAVEN; however, these temperatures are derived from the solar occultation mode and are thus limited to near-terminator conditions (dawn and dusk). The Nadir and Occultation for Mars Discovery spectrometer (Vandaele et al., 2018) on the ExoMars Trace Gas Orbiter (TGO) observes in solar occultation mode in the IR to retrieve CO_2 density and temperature up to 10^{-4} Pa pressure level (∼100 km), but only for the near-terminator region. The temperature and density vertical distribution is also given by the Atmospheric Chemistry Suite (ACS) onboard TGO by using mid-IR solar occultations (Korablev et al., 2018) for a wide altitude range of 20–180 km, but again limited to the near-terminator region. Nonetheless, probing the terminators at dawn and dusk has given a glimpse of the diurnal contrast in temperature (Aoki et al., 2022; Starichenko et al., 2021).

There have also been entry accelerometer observations that measured atmospheric drag during descent of landers through the Martian atmosphere to give temperatures for altitudes ∼10 to 100 km (Seiff & Kirk, 1977; Withers et al., 2002), but, like the MAVEN deep dips, these were confined to a small number of locations and times. On the other hand, there have been numerous orbital accelerometers that give temperature profiles above ∼100 km during aerobraking, however, the altitude, latitude, and local time ranges of these measurements are limited (Siddle et al., 2021; Zurek et al., 2014). A review of these past thermal structure observations for Mars is given in Smith et al. (2017).

The UV stellar occultations of the Spectroscopy for Investigation of Characteristics of the Atmosphere of Mars (SPICAM) instrument aboard the Mars Express (MEX) provided extensive information in the altitude range 70–150 km over a range of local times, but primarily for the nightside (Bertaux et al., 2000; Quémerais et al., 2006). This nightside data set showed large seasonal fluctuations in atmospheric density, response of Martian upper atmosphere to lower atmosphere dust content, southern winter polar warming (Forget et al., 2009), non-migrating tidal signatures in 70–120 km altitude range (Withers et al., 2011), mesospheric CO_2 ice clouds at ∼100 km during southern winter subtropical latitudes (Montmessin et al., 2006), thermal structure in the vicinity of the mesopause (Forget et al., 2009; McDunn et al., 2010; Montmessin et al., 2017), and day/night temperature differences from four midday profiles (Forget et al., 2009). Finally, the diurnal coverage of many other Mars missions is limited by their sun-synchronous orbits: these include Mars Global Surveyor (2 a.m./2 p.m. equator crossing local times) (Smith, 2004b), Mars Odyssey (5 a.m./5 p.m.) (Smith, 2009), and Mars Reconnaissance Orbiter (3 a.m./3 p.m.) (McCleese et al., 2010).

Stellar occultation observations by the IUVS aboard the MAVEN mission are executed in dedicated bimonthly campaigns (Gröller et al., 2018; Jakosky et al., 2015; McClintock et al., 2014) and provide profiles of local densities, temperature, and pressure in the 20–160 km altitude range covering all local times. Of the total 3,003 occultations from March 2015 to January 2022, 53% occur on the nightside and 47% on the dayside. It is the first data set to consistently measure both the dayside and nightside Martian mesosphere. However, because of stray light contamination, analyses to date have been confined to nighttime events (Gröller et al., 2018; Jiang et al., 2019; Nakagawa et al., 2020a, 2020b).

This study makes use of a revised algorithm for removal of stray light from occultation spectra, thereby expanding the useable mission-wide MAVEN/IUVS stellar occultation data set and enabling investigations of diurnal variations in the Martian upper mesosphere/lower thermosphere (∼80 to 160 km) for a range of latitudes, longitudes, and Martian seasons. These methods are presented in Section 2. The observed diurnal, interannual, seasonal, and latitudinal variations in temperature are given in Section 3, followed by the interpretation and discussion of these observations in Section 4, and conclusions of the study in Section 5.

2. Methodology

The execution of the MAVEN/IUVS stellar occultation observations, along with a detailed description of the basic retrieval pipeline, are given by Gröller et al. (2018). Here we describe only the improvements and changes made that enable analysis of more dayside observations.

2.1. Reprocessing the Data Set

Far-ultraviolet 110–190 nm spectra provide densities of CO_2 and O_2 above ~80 km while mid-ultraviolet spectral range between 180 – 340 nm are absorbed by CO_2, O_3, and aerosols generally below ~80 km. Examples of FUV and MUV absorption spectra for a nightside event are shown in Figure S1a in Supporting Information S1, whereas the dayside spectrum is shown in Figure S1b in Supporting Information S1. For most dayside observations, light from the bright Martian disc is scattered internally in the spectrometer that overwhelms the stellar signal and saturates the MUV detector. Stray light contamination of the FUV channel also occurs but is less severe. It does not saturate the FUV detector but usually causes a signal comparable in magnitude to the stellar signal. The prior data-reduction pipeline used to retrieve densities and temperature is quite conservative and rejects any occultations with significant stray light. As a consequence, only a few dayside retrievals are included in the archived results (Gröller et al., 2018). However, as shown in Figure S1b in Supporting Information S1, the FUV stellar signal and the off-order MUV contamination of the FUV stellar signal dominate in separate altitude regions for the majority of the dayside events. The separation between star light and stray planetary light is not always as clear as in Figure S1b in Supporting Information S1, but in most cases it is possible to separate the signals. The FUV spectrum can be processed for such cases if we ignored the contaminated records. Ignoring also the contaminated MUV spectrum and performing the retrievals on only the FUV spectrum for the dayside cases can give valid profiles for these daytime events and considerably expand the useable data set. Instead of using the automatic data pipeline, we have devised a stray light removal algorithm for the FUV analysis. This includes criteria for identifying the contaminated records, determining the altitude range of credible retrievals, etc. Details of identifying valid data range and the retrieval method are given below.

1. Background subtraction: the median background in the FUV spectrum between line of sight (LOS) tangent altitudes 50–120 km is computed. The FUV spectrum at altitudes lower than those used as the background, is eliminated from this analysis, thereby removing the records contaminated by stray light. FUV signal at low altitudes is insignificant, so what is observed is necessarily from the background. This background includes significant signals from atmospheric emissions of H Lyman α at 121.6 nm and OI emissions at 130.4 and 135.6 nm (Gröller et al., 2018). It is a simplified assumption to consider that the background is constant as its variation with altitude is not easily discernible.

2. Atmospheric constituents considered: since FUV star light is predominantly absorbed by CO_2 and O_2, the contribution of both O_3 and aerosols is not considered in the retrieval process. Further, for this study, the abundance of O_2 follows that of CO_2 by considering a constant O_2 mixing ratio of 0.002. We have determined that this assumption has no significant effect on temperature (~1 K) which is derived from CO_2 local density.

3. Limiting the wavelength range: the FUV wavelengths are restricted to 115–170 nm range. Light at wavelengths longward of 170 nm is primarily absorbed by CO_2 at low tangent altitudes where signal-to-noise ratio of the measured spectral transmission is weak because the instrument sensitivity is low. At these high pressure levels, retrieved densities can be significantly underestimated as the stellar spectrum gets fully absorbed in FUV, thus overestimating the temperatures and resulting in a "warm bias" (Montmessin et al., 2017). Additionally, these lower altitudes may be affected by extinction by aerosols which we have chosen not to include in our fitting algorithm.

4. Limiting the altitude range: measurable extinction in the IUVS FUV occultations typically begins near 160 km and light is completely extinguished below 80 km, but the precise limits of good measurements depend on the star and the local atmospheric properties. To determine the altitude range that gives credible retrievals from only FUV, we determine the lower altitude limit where the mean transmission for 118–120 nm reaches 10% of the reference stellar signal, and the upper limit where transmission is 95% for 132–136 nm. An example is shown in Figure S2 in Supporting Information S1.

5. Uncertainties in retrieved temperature: a Monte Carlo approach is used to determine the uncertainties in the retrieved temperature profiles caused by uncertainties in the CO_2 number density (Gröller et al., 2018). The uncertainty in the temperature gradient at the upper boundary can cause higher or lower temperatures. In this

study, due to an assumption of isothermal atmosphere at the upper boundary and, as mentioned earlier, due to possible extinction by aerosols at the lower boundary, the temperature uncertainties at the highest (∼150 to 160 km) and the lowest (∼80 to 90 km) altitudes are generally higher (∼30 K) than at other altitudes (∼3 K). Unlike in the existing data reduction pipeline (Gröller et al., 2018), no smoothing of the CO_2 local density is performed to retrieve temperature.

The Levenberg-Marquardt algorithm is used for fitting the measured FUV transmission spectrum (Gröller et al., 2018) that gives O_2 and CO_2 column (slant) densities along the LOS at each tangent altitude along with the uncertainties of the fitted parameters (Quémerais et al., 2006). Local number densities are then retrieved from these LOS column abundances by Tikhonov regularization (Gröller et al., 2018). From hydrostatic equilibrium and the ideal gas law, temperature and pressure profiles are derived from CO_2 local density with a vertical resolution of around 5 km (Gröller et al., 2018). For the entire reprocessed data set, Figure S3 in Supporting Information S1 shows the retrieved mean CO_2 column density, local density, and temperature for all the observations at local times 3 p.m. and 3 a.m. The day/night differences in these parameters are distinctly seen.

These improvements for FUV analysis are implemented on both dayside and nightside observations. Like the dayside retrievals, the nightside retrievals use only the FUV channel even though the MUV channel is not saturated, resulting in a reprocessed data set with retrievals in ∼80 to 160 km altitude range for all local times. The parameters retrieved for nightside observations using the new algorithm have been tested for consistency with nightside retrievals processed by the existing data pipeline (Gröller et al., 2018) that uses both FUV and MUV spectra. An example is shown in Figure S4 in Supporting Information S1 which demonstrates that the two retrieval processes are consistent and the profiles are within the retrieved uncertainty range, therefore our stray light removal method for FUV can be safely applied on the dayside observations.

2.2. Reprocessed Data Set

Reprocessing the mission-wide MAVEN/IUVS stellar occultation data set by applying the improved stray light removal algorithm for the FUV analysis significantly increased the number of useable observations. The result of this exercise is shown in Figure S5 in Supporting Information S1. While the existing data pipeline (Gröller et al., 2018) processed only 1,403 of the total 3,003 observations, primarily for the nightside (1,114), the improved algorithm added over 1,000 events. This reprocessed data set now includes 1,145 dayside (LT = 6–18) and 1,259 nightside (LT = 18–6) events, thereby enabling the first detailed diurnal study of the Martian upper mesosphere/lower thermosphere in ∼80 to 160 km altitude range.

The coverage of the reprocessed data set is shown in Figure 1 with a wide range of local times, latitudes, and seasons, covering complete Martian years (MYs) 33–35 and MY 36 till the last available observation as of writing (January 2022, Ls = 165°). Unfortunately, even with this expanded data set, there are sparse high latitude observations due to orbital geometry and no events for the southern summer of MY 34. Therefore, observation of thermal structure at the winter poles is not permitted by our data set.

3. Observations

3.1. Diurnal Variations

Figure 2a summarizes the temperature in the Martian upper mesosphere/lower thermosphere as a function of local time and pressure, over all seasons and longitudes, between 65°S and 65°N latitudes for MY 33–36. We consider variations as a function of pressure rather than altitude because pressure is tightly tied to heating and cooling processes, whereas altitude can be affected by unrelated variations in lower atmospheric temperature, for example, during a dust storm. The vertical scale is divided into 30 levels in log-pressure from 10^{-6} to 10^{-2} Pa. The temperature shown is the mean value of all individual temperature measurements that fall within the 1-hr local time and every 0.14 log units of pressure. An approximate geometric altitude is also shown. The altitude scale is defined from the temperature profile averaged over all local times and 5 km altitude bin.

The highest temperatures of ∼250 K are seen during the day (LT = 6–18) at the thermospheric pressure levels below 3×10^{-5} Pa (>130 km), while minimum nightside temperatures are observed to be around 100 K in the mesosphere near 10^{-4} Pa. The temperature rise above the mesopause occurs near 10^{-4} Pa. The dayside is observed
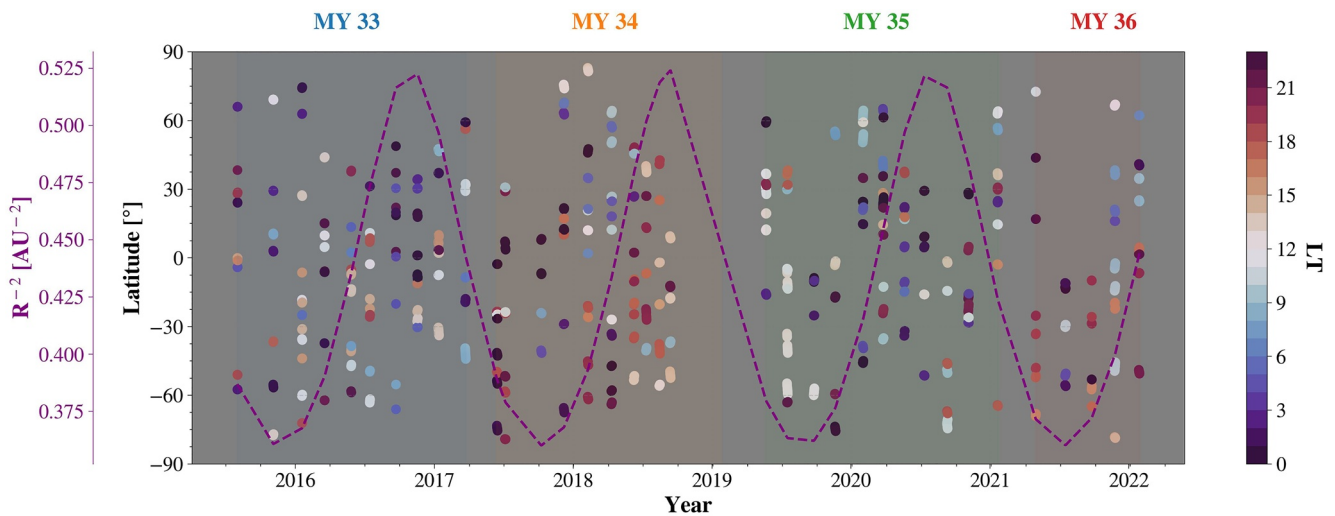
Figure 1. Data coverage of the reprocessed Mars Atmosphere and Volatile EvolutioN/Imaging Ultraviolet Spectrograph stellar occultation observations extending from MY 33 to MY 36. Each data point represents repeated observations for a star at nearly constant latitude and local time but different longitudes. The local time coverage is given by the color of these data points. The purple dashed curve shows the Martian season in terms of the inverse square of the heliocentric distance R in AU^{-2}. The observations show a wide range of local time coverage with sparse high latitude events.
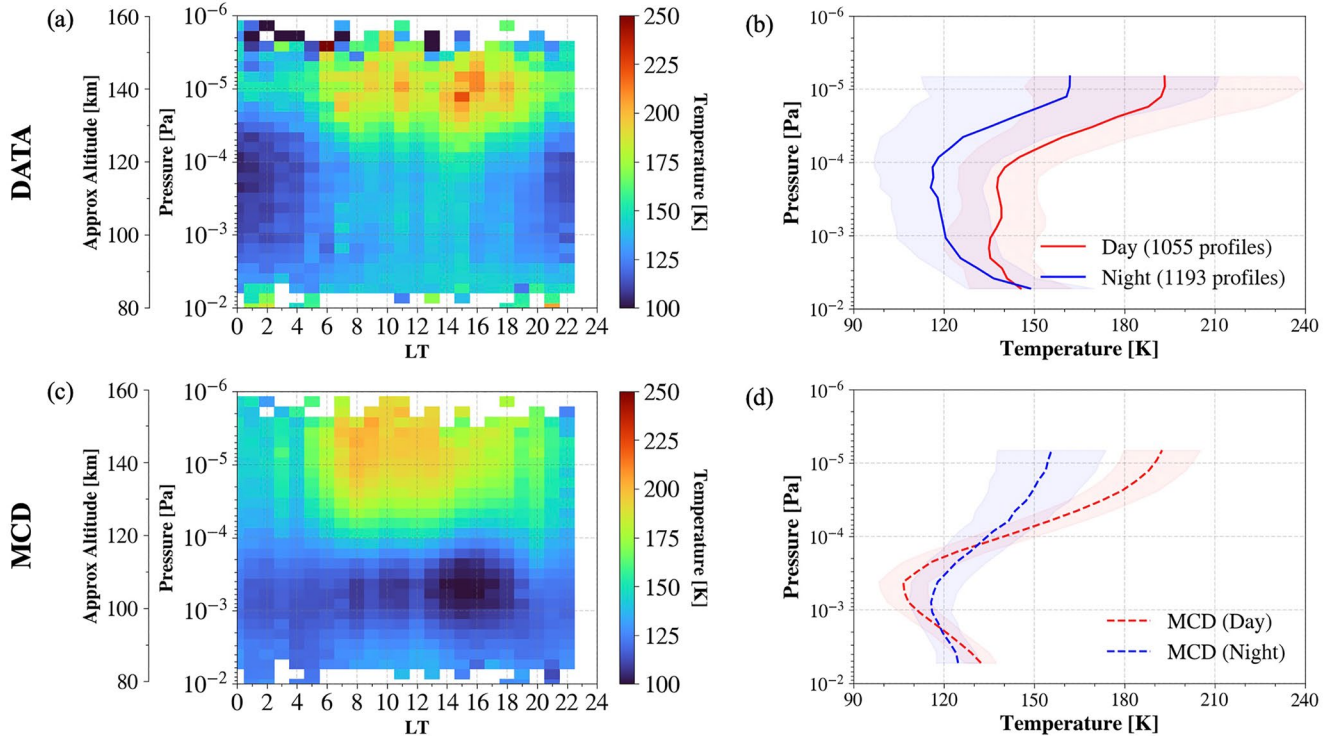

Figure 2. (a) Retrieved average temperature for each pressure-local time bin, along with the approximate geometric altitude. Results are averaged over latitudes from 65°S to 65°N and all seasons, longitudes, and Martians years. (b) Retrieved temperature shown separately for the dayside events in red (LT = 6–18) and the nightside events in blue (LT = 18–6) along with the number of profiles averaged. The shaded areas represent regions of ± 1σ variability in the temperature profile, calculated from all the profiles averaged in that pressure-local time bin and representing the geophysical variation. (c) Mars Climate Database (MCD v5.3) output corresponding to the same geophysical conditions as the observed events in panel (a). (d) Corresponding day and night MCD temperature profiles as in panel (b). The data-model discrepancies are primarily in the vicinity of the mesopause.
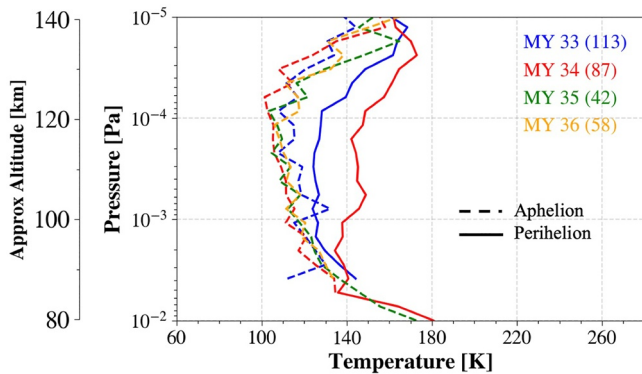
Figure 3. Interannual variations for the aphelion Ls = 60°–90° (dashed curve) and the perihelion Ls = 240°–270° (solid curve) seasons during MY 33 (blue), 34 (red), 35 (green), and 36 (orange). MY 35 and 36 cover only the aphelion season. Also shown are the number of profiles for each MY. These profiles for the two seasons are averaged over all longitudes and local times, for latitudes 65°S–65°N.

to be uniformly warmer than the nightside at all observed pressure levels. Diurnal variations are seen to be the largest in the thermosphere, moderate in the mesosphere, and smallest at higher pressure levels. Overall, these temperatures are consistent with earlier results of the thermosphere in this altitude range (Forget et al., 2009; Jain et al., 2021; Stone et al., 2018; Thiemann et al., 2018).

Figure 2b shows the dayside and the nightside vertical temperature profiles averaged over the entire reprocessed data set for latitudes 65°S–65°N and averaged over all seasons and longitudes. Similar to Figure 2a, the day/night differences in the Martian thermal structure are evident here, especially at pressure levels lower than 2×10^{-3} Pa (above 90 km) where the effect of solar forcing increases with altitude. The observed nightside is cooler than the dayside by maximum ~30 K at altitudes above 10^{-4} Pa level (>120 km). There is a monotonic increase in both nightside and the dayside temperatures with altitude in the lower thermosphere. A well-defined nighttime mesopause reaching 115 K is observed, while the dayside mesosphere is warm and approximately isothermal at around 135 K, resulting in a day/night difference of 20 K around the mesopause.

Uncertainties in temperature for individual profiles are typically small and discussed extensively in Gröller et al. (2018). For these average profiles, the real variability within each pressure-local time bin is usually much larger than the temperature errors. The only exceptions to this are for pressure levels lower than 5×10^{-6} Pa, where the uncertainty in the upper boundary dominates, and at pressure levels higher than 5×10^{-3} Pa where our neglect of aerosol extinction may cause errors in the derived temperature. For this reason, the temperature profiles are shown in $5 \times 10^{-6} - 5 \times 10^{-3}$ Pa range.

The nightside temperature profile is consistent with the MEX/SPICAM results in Figure 14 of Montmessin et al. (2017) showing nightside mesopause temperature of ~110 K and thermospheric temperature reaching 160 K at ~140 km. The shape of the dayside profile is also similar to that found by MEX/SPICAM in Figure 9 of Forget et al. (2009). They reported four midday temperature profiles for MY 27 (Ls = 270°–330°, latitude = 40°–50°N) and showed the mean dayside temperatures to be 15 K warmer than midnight at altitudes above 2×10^{-3} Pa level (~110 km), with the observed differences being consistent with propagating thermal tides and variations in local solar heating. They also showed smaller diurnal differences at altitudes below 2×10^{-3} Pa level. Comparison with model predictions shown in Figures 2c and 2d are discussed later in Section 4.2.

3.2. Interannual Variations

Figure 3 shows the average temperature profiles for MY 33 to MY 36, for two separate Martian seasons, that is, aphelion (Ls = 60°–90°) and perihelion (Ls = 240°–270°), between 65°S and 65°N latitudes. These two seasons differ because of the obliquity of Mars and the strong variation of solar insolation and dust storm activity associated with the orbital eccentricity of Mars. Mars is 20% closer to the Sun at perihelion with 40% greater solar insolation than at aphelion. Only aphelion data are available for MY 36 as of writing. Also, no perihelion observations are available for MY 35 for this solar longitude and latitude range. These profiles are averaged over all local times. The profiles look stable and repeatable for different MYs. Similar temperature profiles are seen near aphelion for all the MYs. These aphelion profiles show decrease in temperature in the mesosphere as the altitude increases, with temperature at the mesopause near 10^{-4} Pa reaching 100 K. In contrast, the interannual differences are observed to be predominant around the perihelion, and are the largest in the upper mesosphere above ~90 km. The perihelion profiles show approximately isothermal mesosphere. The maximum mesospheric temperature (~150 K) for this altitude range is seen for the perihelion season of MY 34 when the decaying phase of a planet encircling dust event (PEDE) was observed, resulting in the seasonal differences of ~40 K for that year, whereas weaker seasonal variation of ~15 K is seen for MY 33. Jain et al. (2020) showed an increase in dayside temperature at ~170 km by 20 K after the onset of MY 34 PEDE due to modification in the zonal and
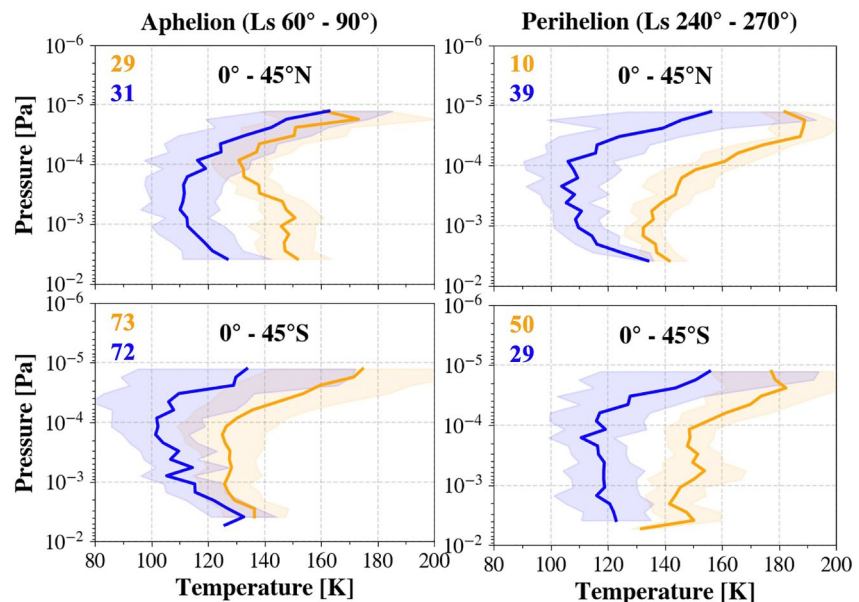
Figure 4. Seasonal, latitudinal, and diurnal variations in the retrieved temperatures, averaged and shown separately for the aphelion season in the left column and for the perihelion season in the right column. For both the seasons, top panels are for the northern low latitude events (0°–45°N) and the bottom panel is for the southern latitudes (0°–45°S), while the dayside observations are shown in orange and the nightside events are in blue. The respective colored numbers represent the number of profiles averaged.

meridional winds at the thermospheric altitudes and damping of the mean circulation by the dust storm development (González-Galindo et al., 2015).

3.3. Seasonal and Latitudinal Variations

Figure 4 shows the temperature profiles for the dayside and the nightside observations, separately for the northern (top panels) and the southern (bottom panels) hemispheres in order to investigate the diurnal differences between solstices. The dayside profiles are always warmer than the nightside at all observed pressure levels. These diurnal differences reach a maximum ~40 K in the mesosphere for the summer latitudes in both the hemispheres. A minimum nightside mesopause temperature of ~100 K is seen near 10^{-4} Pa for the winter latitudes in both the hemispheres, while the perihelion southern latitudes (around southern summer dust storm season) exhibit the maximum mesospheric temperatures of 150 K during the daytime. Both day and night temperatures are the coldest for the southern winter around aphelion, and warmest for the southern summer around the perihelion season. That is, the effects of increased solar insolation around perihelion are clearly reflected in the temperature profiles. We have perihelion observations only for MYs 33 and 34. Any possible influence of the MY 34 PEDE is tested by separating MY 33 and MY 34 observations (not shown). The nightside profiles (39 events) for northern hemisphere perihelion are only from the MY 33 while the dayside profiles (10 events) are only from the MY 34. Therefore, excluding the global dust storm period only had a significant effect on the northern winter daytime profiles due to the data availability. For this reason, the interannual perihelion difference during MY 33 and 34 in Figure 3 is primarily due to the dayside observations that are present only for the MY 34. Further, an inverse diurnal variation for northern hemisphere aphelion season (top left) seems to be due to the data sampling. The nightside events have almost equal number of observations for latitudes 0°–10°N and for latitudes 30°–45°N. On the other hand, the dayside observations have majority of observations for latitudes 30°–45°N.

Our nightside seasonal/latitudinal variations compare well with the MEX/SPICAM nightside observations (Montmessin et al., 2017). These day/night temperature profiles around aphelion in left panels of Figure 4 are also consistent with Figure 11 of Bougher et al. (2015) that shows the accelerometer measured equatorial temperature profiles on altitude scale 100–200 km from MRO and MGS, and MGITM simulations. They also showed the aphelion nightside mesopause temperature around 100 K and dayside mesopause at ~120 K, with day and
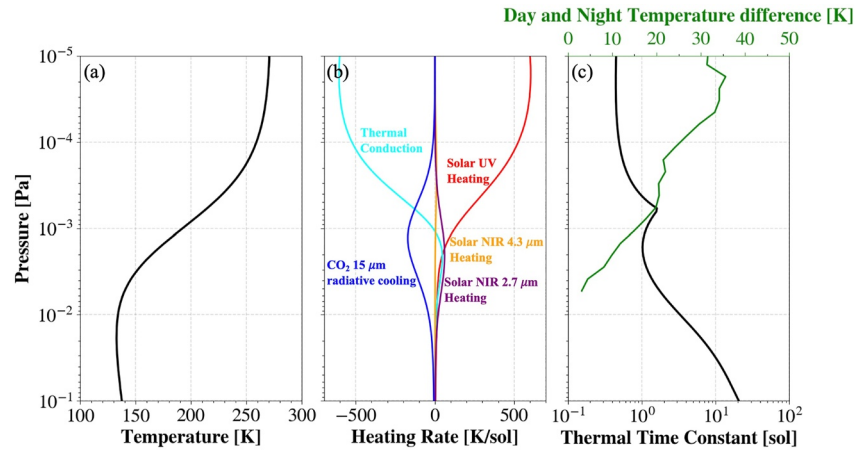
Figure 5. (a) The calculated 1-D model global-mean temperature profile, (b) heating rates, and (c) the thermal time constant in black and the retrieved day and night temperature differences in green.

night thermospheric temperatures at ~140 km (near 10^{-5} Pa) reaching 180 and 140 K, respectively. In summary, the seasonal and latitudinal variations of the diurnal cycle exhibit expected characteristics, and out of all the variations, the diurnal are the most dominant.

4. Discussion

The observations reveal a strong diurnal variation with dayside temperatures warmer than the nightside for any combination of season and latitude, and these day/night differences become more prominent as the altitude increases above 2×10^{-3} Pa level (~90 km). The observed temperature profiles suggest strong radiative control. We next investigate this in more detail.

4.1. Radiative Time Constants

To look into the primary drivers of the Martian thermal structure at these altitudes, Figure 5 shows the temperature profile along with the heating and cooling rates from a global-average 1-D numerical model. Solar heating rates in the UV are calculated assuming a heating efficiency of 20% (Fox et al., 1996; Yelle et al., 2014). Heating rates in the 2.7 and 4.3 μm near-IR bands are based on CO_2 line lists from HITRAN (Gordon et al., 2017) and correlated-k coefficients. It is assumed that all absorbed energy is converted to heat; vibrational interchange among excited levels is not included in the calculations. Cooling in the 15 μm CO_2 band is also based on the HITRAN line lists but using a line-by-line calculation and Spectral Mapping Transformations (West et al., 1990; Yelle et al., 1991). It is the O-CO_2 collision that excites the CO_2 vibrational state in 15 μm band, whose IR emission results in radiative cooling (Bougher et al., 1994). The calculations include a full non-LTE treatment of the 15 μm band using techniques described in Yelle et al. (1991). We adopt a rate of 3×10^{-12} $cm^3 s^{-1}$ for collisional de-excitation of the ν_2 vibrational level of CO_2 (Bougher & Roble, 1991). The calculations include thermal conduction while the dynamical terms in the energy balance equation are not considered. The calculations are described in more detail in Yelle et al. (1991, 2014).

Our goal in construction of these 1-D models is to investigate the thermal time constants in the upper mesosphere and thermosphere. These thermal time constants are estimated as,

$$t = {}^{c_p \rho T}/_Q \tag{1}$$

where ρ is the number density of the atmosphere, c_p is the specific heat capacity at constant pressure, T is the temperature, and Q is the radiative cooling rate in the 15 μm band. This is an estimate of the Newtonian cooling rate. The radiative effects from dust are not considered, therefore, the thermal time constants at higher pressure levels (~80 km) may be slightly overestimated. However, this aerosol heating at 80 km doesn't affect the radiative time constant at 105 km. Results are shown in Figure 5c.

The calculated temperature profile in Figure 5a matches the observations fairly well with a temperature of 150 K near 3×10^{-3} Pa, a mesopause temperature of ~130 K, and a warm lower thermosphere reaching 250 K. From the modeled global-mean heating rates in Figure 5b, it is expected that the thermal balance in the lower thermosphere is primarily between solar UV heating and thermal conduction while the mesosphere is governed by the radiative processes with a balance between solar NIR heating and CO_2 15 μm radiative cooling. Similar conclusions have been found in many previous studies of the thermal balance in this region (cf., Bougher et al., 1999).

The thermal time constants in Figure 5c are significantly longer than a Mars day (1 sol) at pressures greater than 3×10^{-3} Pa and significantly shorter than a Mars day at pressures less than 3×10^{-4} Pa. Thus, we expect little diurnal variations at pressures greater than 3×10^{-3} Pa but larger diurnal variations at pressures less than 3×10^{-4} Pa. The strong diurnal variations of temperature at low pressure is well established (Bougher et al., 1990, 2015; Stone et al., 2018) as is the weaker diurnal variations at pressures greater than 3×10^{-3} Pa (Forget et al., 2009; Lee et al., 2009). The atmospheric region between 3×10^{-4} and 3×10^{-3} Pa has not been explored much but is quite interesting as it contains the mesopause and because the thermal time constant is of the order of 1 sol.

The observed day/night differences are also shown in Figure 5c along with the 1-D model thermal time constant. These diurnal differences are deduced from Figure 2b and are consistent with expectations based on the radiative time constants. This suggests that the diurnal variations in the upper mesosphere/lower thermosphere are primarily due to diurnally varying solar heating.

4.2. Comparison With the Mars Climate Database

We have also compared our results with the Mars Climate Database (MCD v5.3), which is based on the Mars Planetary Climate Model (PCM), formerly known as the Laboratoire de Météorologie Dynamique Mars Global Climate Model (LMD MGCM). We use the MCD v5.3 climatological dust scenario under average solar EUV conditions (Forget et al., 1999; González-Galindo et al., 2015; Millour et al., 2018). Figure 2a shows the observed diurnal variations as described earlier in Section 3.1, along with the MCD temperature output in Figure 2c following the same sampling as the data, making Figure 2c directly comparable to Figure 2a. It is seen that the MCD matches the observed upper atmospheric temperatures and their variation quite well with a dayside maximum of roughly 250 K and a nightside minimum of around 150 K. However, the local time of the maximum temperature in the thermosphere appears to be inconsistent with the data. The observations show the maximum temperature in the mid-afternoon (~3 p.m.) while the maximum in the MCD is in the morning (~7 a.m. to 8 a.m.). The location of the temperature maximum inferred from the occultation data is consistent with that inferred from MAVEN mass spectrometer measurements (Stone et al., 2018).

The 1-D global mean numerical model was found to be consistent with the observations, showing a radiative balance around the mesopause with thermal time constant of the order of 1 sol, even though it ignores the dynamical terms in the energy balance equation. The most important dynamical effect is likely to be adiabatic heating/cooling associated with vertical winds. We can estimate the magnitude of the vertical wind w required for adiabatic heating/cooling to compete with solar heating from,

$$w \sim Q/c_p \rho S \tag{2}$$

where S is the static stability of the atmosphere. For the $P = 3 \times 10^{-4}$ Pa level, which is the region of the strong thermospheric temperature gradient as shown in Figure 5, we have $Q/c_p \rho \sim 300 \, \text{K/sol} \sim 3.4 \times 10^{-3} \, \text{K/s}$. To estimate S, we approximate it as the dry adiabatic lapse rate such that $S \sim g/c_p \sim 4.5 \, \text{K/km}$ implying $w \sim 75 \, \text{cm/s}$. This is within the range predicted by GCM simulations (Bougher et al., 1990; González-Galindo, Forget, López-Valverde, & Angelats I Coll, 2009).

The reason for a temperature maximum in the morning in the MCD simulations is not clear but is likely related to these dynamical processes. As discussed in Stone et al. (2018), the late afternoon maximum in thermospheric temperature is a result of the dependence of solar heating on solar zenith angle and the thermal inertia of the upper atmosphere. We note that Bougher et al. (2014) predicts a thermospheric temperature maximum in the afternoon. The level of the thermospheric temperature rise in MCD near 10^{-4} Pa matches well with the data. Moreover, both model and data show small diurnal variations at pressure levels greater than 2×10^{-3} Pa and the

temperature values are consistent. However, a quite conspicuous discrepancy is seen between the data and the model in the 2×10^{-4} to 2×10^{-3} Pa pressure range. That is, in the mesosphere, the MCD predicts a temperature minimum on the dayside and maximum on the nightside, opposite to the observations.

To further investigate these diurnal discrepancies, Figure 2d shows the day and night vertical temperature profiles from the MCD. The profiles corresponding to the data in Figure 2b were previously discussed in Section 3.1. It is seen that the predicted day and night profiles are consistent with the observed profiles at the thermospheric altitudes of pressure less than 2×10^{-5} Pa showing strong diurnal temperature variations. Furthermore, both data and the model show weak diurnal variations at lower altitudes. However, the data-model differs significantly in the mesosphere with the MCD dayside mesopause cooler than the observed mesosphere by ∼35 K, and also cooler than the predicted nightside mesopause by ∼10 K. In the 2×10^{-4} to 2×10^{-3} Pa region, the data shows a dayside maximum of 138 K near 3 p.m. and a nightside minimum of 103 K near midnight. The MCD has a dayside minimum of ∼100 K near 3 p.m. and a nightside maximum of 120 K near midnight. It is also important to note here that the observed maximum day/night temperature difference of ∼20 K in the mesosphere is much larger and opposite in trend than that given by the MCD. To see how well the mesospheric thermal structure is reproduced by the MCD during a PEDE, we compared the retrieved temperature profiles for MY 34 (Ls = 180°–270°) with the climatological MCD values as well as with the dust storm MCD scenario values that represent Mars during a global dust storm (dust opacity $\tau = 5$) (not shown). We found a difference of ∼5 to 10 K at the mesopause between the two model outputs but both these dust scenarios predicted the dayside mesopause to be cooler than the observations and unable to reproduce the observed thermal structure during the MY 34 PEDE. The largest data-model discrepancy in Figure 2d is seen in the vicinity of the mesopause. The nighttime predicted mesopause is warmer and lower in altitude than the observed nighttime mesopause.

The difference between the observed and calculated mesopause altitude was also shown by Forget et al. (2009) and McDunn et al. (2010) by using the nightside MEX/SPICAM stellar occultation temperature profiles. The GCM parameterization of the cooling due to CO_2 15 μm emissions by considering a constant atomic oxygen profile under NLTE was suggested to be likely responsible for these differences (González-Galindo, Forget, López-Valverde, Angeláis I Coll, & Millour, 2009; González-Galindo et al., 2005). Later, González-Galindo et al. (2013) described improvements in the LMD MGCM, including improved 15 μm cooling parameterization by using actual atomic oxygen profile calculated by the model instead of a constant one. Montmessin et al. (2017) later showed the altitude of the nightside mesopause inferred from the MEX/SPICAM measurements to be in better agreement with the updated GCM. Now that the dayside observations are also available for a similar altitude range, it is interesting to see that these data-model discrepancies at the dayside mesopause are even larger and opposite in trend than the nightside differences. That is, the dayside mesopause is predicted to be cooler and higher in altitude than the observed mesopause.

The most likely explanation for a nightside mesosphere warmer than the dayside is for the diurnal variations driven by radiation to be overwhelmed by tidal variations. We are considering migrating (sun-synchronous) tides because we are averaging over all longitudes and examining variations with local time (Forbes, 2004; Zurek, 1976). On the other hand, because the tides are damped by radiation (Smith, 2004a), a short radiative time constant (∼1 sol) means both strong radiative forcing of diurnal variations and strong damping of upward propagating tides, suggesting that the tides near the Martian mesopause could be relatively weak. The fact that the data shows the dayside mesosphere to be always warmer than the nightside at all pressure levels suggests that migrating tides in the MCD are too strong in this pressure range.

To investigate this further, Figure 6 shows deviations from the diurnal mean for observed and MCD temperatures in 65°S–65°N latitude range for southern spring equinox and for all MYs. Figure 6a shows the average temperature deviations in pressure-local time bins for this season and latitude range as given by the MCD. A clear signature of a westward propagating semidiurnal migrating tide with a downward propagating phase (upward energy flow) is seen for the upper mesosphere (pressure higher than 10^{-4} Pa). Around this pressure level (∼120 km) there is a transition from this vertically propagating semidiurnal thermal tide to a strong diurnal tide in the lower thermosphere with a fixed local-time variation. The 10^{-4} Pa pressure level is around the same location as the rise in thermospheric temperature above the mesopause in Figure 2a. To more clearly compare with the observations, Figure 6b shows the temperature deviations in the MCD simulations sampled in the same manner as the observations. The actual data coverage in terms of the solar longitude, latitude, and local time for this season is shown in Figure 6d. The data coverage is limited, therefore, the tidal crest around midnight in Figure 6b is not
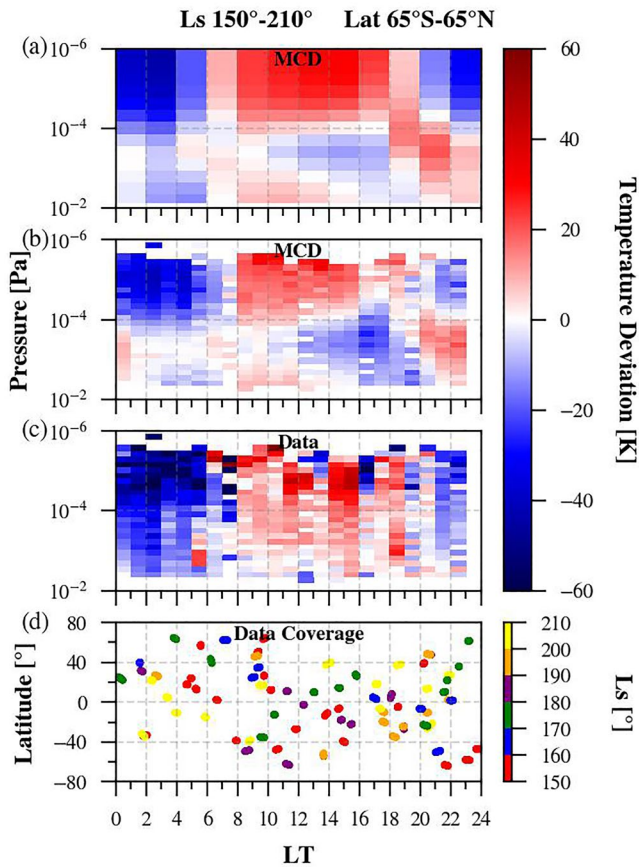
Figure 6. Temperature deviations from the diurnal mean for (a) Mars Climate Database (MCD v5.3) temperature output in each of the local time-pressure bins around the southern spring equinox averaged for Ls 150°–210° and latitudes 65°S–65°N, (b) temperature deviations given by the MCD corresponding to the observed data coverage, (c) retrieved temperature deviations for this Martian season and latitude range, and (d) the data coverage in this range. The model shows a vertically propagating semidiurnal tide in the upper mesosphere with downward phase progression. The data shows no clear semidiurnal tidal component but a diurnal one.

seen in Figure 6a, even though both are based on the MCD outputs, because it has contribution from only latitude ∼20°N. On the other hand, Figure 6c shows the corresponding observed temperature deviations. The data shows no clear semidiurnal migrating tidal component, but a diurnal tide with a fixed local-time variation and no vertical phase shift.

The data with and without MY 34 (Ls = 150°–210°) (not shown) also show no clear semidiurnal migrating tides in the upper mesosphere, as opposed to the signatures exhibited by the MCD following the same data sampling. This indicates that the global dust storm during MY 34 may not affect the tidal analysis presented in Figure 6. A similar analysis was carried out for all other seasons and latitudes, and the dayside is always observed to be warmer than the nightside at all altitudes, that is, the data does not show a meaningful signature of migrating tides that could corroborate the MCD. The data shows that regions at pressure levels lower than 2×10^{-3} Pa (>90 km) are under strong solar control. This is consistent with short radiative time constant discussed earlier.

Previous measurements of the migrating tides on Mars are limited to altitudes below 80 km (González-Galindo, Forget, López-Valverde, & Angelats I Coll, 2009). These tidal signatures in the lower atmosphere of Mars are quite strong and have been extensively studied. Lee et al. (2009) showed a diurnal thermal tide to dominate for all latitudes and Martian seasons in the middle atmosphere (35–80 km). Further, due to these strong tidal forcing and relatively weak dissipation from molecular conduction and viscosity, semidiurnal tides are predicted to be a major component for Mars circulation up to 80 km altitude with amplitudes increasing with dust loading (Kleinböhl et al., 2013).

Bougher et al. (1993) assumed a strong tide at 100 km and found that it was still strong enough to overwhelm the diurnal variation up to 135 km. They adapted the terrestrial scheme to a Mars model appropriate to Mariner 9 near-solar-minimum conditions and presented the MTGCM simulations with and without the tidal forcing. They assumed a dominant (2, 2) semidiurnal tide at their lower boundary of 100 km (estimated amplitude ∼20 K) and showed a temperature perturbation of ±22.5 K at the mesopause (∼110 km). They showed the semidiurnal features driven by (2, 2) tide to be prevalent in the Martian atmosphere below ∼135 km with peak tidal amplitude of 27 K above 125 km, and a solar driven diurnal component dominant above 135 km.

This appears generally consistent with the MCD predictions but in conflict with the observations presented here: Apparently, semidiurnal migrating tides on Mars do not seem to propagate to the upper mesosphere/lower thermosphere as efficiently as predicted by these models. Propagation of tides is complicated, depending on the zonal wind profile, radiative damping rates, and damping by viscosity and thermal conduction; therefore, further investigation is needed to understand what is limiting the propagation of these tides to this altitude region on Mars.

4.3. Comparison With Earth

It is interesting to compare our findings for Mars with what we know about tides and thermal structure near the mesopause on Earth. The observed diurnal mean at terrestrial mesopause is around 200 K (States & Gardner, 2000) while the day and night Martian mesopause average temperatures are around 100 and 140 K, respectively, quite low as compared to Earth. As for the composition, the terrestrial mesopause is dominated by well-mixed N_2 and O_2, and reactive species O and H, while CO_2 is a minor species that is affected by molecular diffusion and transport by mean circulation (Smith, 2004a and references therein). Additionally, both O and H become long-lived in terrestrial MLT region (mesosphere/lower thermosphere ∼60 to 110 km altitude range). On the other hand, CO_2 is a major species on Mars. For Earth, it is suggested that the observed mean MLT thermal structure is largely consistent with the assumption of radiative balance between direct solar UV heating and radiative cooling by IR

emission (States & Gardner, 2000). It was shown in Figure 5 that the Martian mesosphere is also dominated by radiative balance, that is, Earth's mesopause, like that of Mars, is cooled primarily by the CO_2 15 μm band.

The radiative cooling rate at the terrestrial mesopause is approximately 20 K/day (Bougher et al., 1994) and the mesopause temperature, 200 K. The time constant for radiative cooling is therefore ∼10 Earth days, compared with ∼1 sol for Mars. Due to all these factors, Earth's mesopause temperature is larger than Mars' and also exhibits smaller diurnal variations than that observed for Mars. Further, States and Gardner (1998) showed propagating tidal oscillations for the terrestrial upper mesosphere (80–110 km) to be significant, that is, on Earth the temperature variations due to tides is quite large in the mesosphere, whereas propagating tidal signatures are not detectable and significantly smaller in amplitude in the Martian observations, consistent with the respective radiative time constants.

5. Conclusions

By applying the improved stray light removal algorithm for the FUV analysis to reprocess the mission-wide MAVEN/IUVS stellar occultation data set from March 2015 to January 2022, we have been able to add ∼1,000 dayside observations in the processed database, therefore enabling the first detailed study of the diurnal thermal structure of Martian upper mesosphere/lower thermosphere for $10^{-5} - 10^{-2}$ Pa pressure levels (∼80 to 160 km altitude range). The following conclusions can be drawn from this study,

1. Prominent diurnal variations are seen in the data with the dayside warmer than the nightside at all observed pressure levels.
2. The maximum day/night difference of ∼30 K is seen in the lower thermosphere at pressure levels lower than 3×10^{-5} Pa (>130 km), variation of ∼20 K is seen in the vicinity of the mesopause, while little diurnal variations are seen at lower altitudes.
3. The migrating tidal signatures are significantly smaller in amplitude and not detected in the data. Instead, data shows that the regions at pressure levels lower than 2×10^{-3} Pa (>90 km) are under strong solar control.
4. The global-mean 1-D numerical model corresponds to the observed diurnal temperature trends surprisingly well and shows that the thermal structure of the Martian upper mesosphere is consistent with short radiative time constant.
5. The radiative time constant around Martian mesopause is of the order of 1 Mars day with moderate diurnal differences. In contrast, the diurnal variations at the terrestrial mesopause are known to be insignificant. The temperature variations due to tides is quite large in the Earth's mesosphere with radiative time constant of around 10 Earth days at the mesopause.
6. The Mars Climate Database shows an opposite diurnal trend in the mesosphere, with the dayside mesopause cooler than the nightside by ∼10 K, along with signatures of a vertically propagating tide.

The MAVEN/IUVS stellar occultation reprocessed data set provides an unprecedented constraint on the structure of the Martian mesosphere. We have not only been able to establish for the first time how the Martian mesopause varies on a diurnal scale, but also found that the model predictions are inconsistent with the observations. The models do not match the diurnal variations that are observed around the mesopause, showing that our current understanding of the dynamics and structure of this important region is inadequate. Further examination of the zonal wind profile, radiative damping rates, and damping by molecular viscosity and thermal conduction may shed light on the issues.

Data Availability Statement

The MAVEN/IUVS calibrated (level 1B) stellar occultation data (Schneider, 2022) are publicly available in FITS format on the NASA Planetary Data System (PDS) at https://atmos.nmsu.edu/PDS/data/PDS4/MAVEN/iuvs_calibrated_bundle/l1b/occultation/, identified by "occultation" with version/revision tag v13_r01. The data are also publicly available on the LASP MAVEN Science Data Center (SDC, https://lasp.colorado.edu/maven/sdc/public/). Data used in this study, that includes retrievals from the reprocessed stellar occultation data set and 1-D model output, can be downloaded from the CU Scholar data repository (Gupta, 2022). The Mars Climate Database version 5.3 Web Interface is publicly available at http://www-mars.lmd.jussieu.fr/mcd_python/. The full version of its access software can be requested at http://www-mars.lmd.jussieu.fr/mars/MCD_pro/mcd_pro.html.

References

Aoki, S., Gkouvelis, L., Gerard, J.-C., Soret, L., Hubert, B., Lopez-Valverde, M. A., et al. (2022). Density and temperature of the upper mesosphere and lower thermosphere of Mars retrieved from the OI 557.7 nm dayglow measured by TGO/NOMAD. *Journal of Geophysical Research: Planets*, *127*(6), 1–12. https://doi.org/10.1029/2022JE007206

Bertaux, J. L., Fonteyn, D., Korablev, O., Chassefière, E., Dimarellis, E., Dubois, J. P., et al. (2000). The study of the Martian atmosphere from top to bottom with SPICAM light on Mars Express. *Planetary and Space Science*, *48*(12–14), 1303–1320. https://doi.org/10.1016/s0032-0633(00)00111-2

Bougher, S. W., Cravens, T. E., Grebowsky, J., & Luhmann, J. (2014). The aeronomy of Mars: Characterization by MAVEN of the upper atmosphere reservoir that regulates volatile escape. *Space Science Review*, *195*(1–4), 423–456. https://doi.org/10.1007/s11214-014-0053-7

Bougher, S. W., Engel, S., Roble, R. G., & Foster, B. (1999). Comparative terrestrial planet thermospheres: 2. Solar cycle variation of global structure and winds at equinox. *Journal of Geophysical Research*, *104*(7), 16591–16611. https://doi.org/10.1029/1998JE001019

Bougher, S. W., Fesen, C. G., Ridley, E. C., & Zurek, R. W. (1993). Mars mesosphere and thermosphere coupling: Semidiurnal tides. *Journal of Geophysical Research*, *98*(E2), 3281–3295. https://doi.org/10.1029/92je02727

Bougher, S. W., Hunten, D. M., & Roble, R. G. (1994). CO2 cooling in terrestrial planet thermospheres. *Journal of Geophysical Research*, *99*(7), 14609–14622. https://doi.org/10.1029/94JE01088

Bougher, S. W., Pawlowski, D., Bell, J. M., Nelli, S., McDunn, T., Murphy, J. R., et al. (2015). Mars Global Ionosphere-Thermosphere Model: Solar cycle, seasonal, and diurnal variations of the Mars upper atmosphere. *Journal of Geophysical Research: Planets*, *120*(2), 311–342. https://doi.org/10.1002/2014JE004715

Bougher, S. W., & Roble, R. G. (1991). Comparative terrestrial planet thermospheres: 1. Solar cycle variation of global mean temperatures. *Journal of Geophysical Research*, *96*(A7), 11045. https://doi.org/10.1029/91ja01162

Bougher, S. W., Roble, R. G., Ridley, E. C., & Dickinson, R. E. (1990). The Mars thermosphere: 2. General circulation with coupled dynamics and composition. *Journal of Geophysical Research*, *95*(B9), 14811. https://doi.org/10.1029/jb095ib09p14811

Forbes, J. M. (2004). Tides in the middle and upper atmospheres of Mars and Venus. *Advances in Space Research*, *33*(2), 125–131. https://doi.org/10.1016/j.asr.2003.05.007

Forget, F., Hourdin, F., Fournier, R., Hourdin, C., Talagrand, O., Collins, M., et al. (1999). Improved general circulation models of the Martian atmosphere from the surface to above 80 km. *Journal of Geophysical Research*, *104*(E10), 24155–24175. https://doi.org/10.1029/1999JE001025

Forget, F., Montmessin, F., Bertaux, J. L., González-Galindo, F., Lebonnois, S., Quémerais, E., et al. (2009). Density and temperatures of the upper Martian atmosphere measured by stellar occultations with Mars Express SPICAM. *Journal of Geophysical Research*, *114*(1), 1–19. https://doi.org/10.1029/2008JE003086

Fox, J. L., Zhou, P., & Bougher, S. W. (1996). The Martian thermosphere/ionosphere at high and low solar activities. *Advances in Space Research*, *17*(11), 203–218. https://doi.org/10.1016/0273-1177(95)00751-Y

González-Galindo, F., Chaufray, J. Y., Lõpez-Valverde, M. A., Gilli, G., Forget, F., Leblanc, F., et al. (2013). Three-dimensional Martian ionosphere model: I. The photochemical ionosphere below 180 km. *Journal of Geophysical Research: Planets*, *118*(10), 2105–2123. https://doi.org/10.1002/jgre.20150

González-Galindo, F., Forget, F., López-Valverde, M. A., Angeláis I Coll, M., & Millour, E. (2009). A ground-to-exosphere Martian general circulation model: 1. Seasonal, diurnal, and solar cycle variation of thermospheric temperatures. *Journal of Geophysical Research*, *114*(4), 1–21. https://doi.org/10.1029/2008JE003246

González-Galindo, F., Forget, F., López-Valverde, M. A., & Angelats I Coll, M. (2009). A ground-to-exosphere Martian general circulation model: 2. Atmosphere during solstice conditions – Thermospheric polar warming. *Journal of Geophysical Research*, *114*(8), 1–21. https://doi.org/10.1029/2008JE003277

González-Galindo, F., López-Valverde, M. A., Angelats i Coll, M., & Forget, F. (2005). Extension of a Martian general circulation model to thermospheric altitudes: UV heating and photochemical models. *Journal of Geophysical Research*, *110*(9), 1–17. https://doi.org/10.1029/2004JE002312

González-Galindo, F., Lõpez-Valverde, M. A., Forget, F., García-Comas, M., Millour, E., & Montabone, L. (2015). Variability of the Martian thermosphere during eight Martian years as simulated by a ground-to-exosphere global circulation model. *Journal of Geophysical Research: Planets*, *120*(11), 2020–2035. https://doi.org/10.1002/2015JE004925

Gordon, I. E., Rothman, L. S., Hill, C., Kochanov, R. V., Tan, Y., Bernath, P. F., et al. (2017). The HITRAN2016 molecular spectroscopic database. *Journal of Quantitative Spectroscopy and Radiative Transfer*, *203*, 3–69. https://doi.org/10.1016/j.jqsrt.2017.06.038

Gröller, H., Montmessin, F., Yelle, R. V., Lefèvre, F., Forget, F., Schneider, N. M., et al. (2018). MAVEN/IUVS stellar occultation measurements of Mars atmospheric structure and composition. *Journal of Geophysical Research: Planets*, *123*(6), 1449–1483. https://doi.org/10.1029/2017JE005466

Gupta, S. (2022). Thermal structure of the Martian upper mesosphere/lower thermosphere from MAVEN/IUVS stellar occultations [data] [Dataset]. University of Colorado Boulder. https://doi.org/10.25810/Z1WY-CQ62

Haberle, R. M., Clancy, R. T., Forget, F., Smith, M. D., & Zurek, R. W. (Eds.) (2017). *The atmosphere and climate of Mars*. Cambridge University Press. https://doi.org/10.1017/9781139060172

Jain, S. K., Bougher, S. W., Deighan, J., Schneider, N. M., González Galindo, F., Stewart, A. I. F., et al. (2020). Martian thermospheric warming associated with the planet encircling dust event of 2018. *Geophysical Research Letters*, *47*(3), 1–9. https://doi.org/10.1029/2019GL085302

Jain, S. K., Soto, E., Evans, J. S., Deighan, J., Schneider, N. M., & Bougher, S. W. (2021). Thermal structure of Mars' middle and upper atmospheres: Understanding the impacts of dynamics and of solar forcing. *Icarus*, 114703. https://doi.org/10.1016/j.icarus.2021.114703

Jakosky, B. M., Lin, R. P., Grebowsky, J. M., Luhmann, J. G., Mitchell, D. F., Beutelschies, G., et al. (2015). The Mars atmosphere and volatile evolution (MAVEN) mission. *Space Science Reviews*, *195*(1–4), 3–48. https://doi.org/10.1007/s11214-015-0139-x

Jiang, F. Y., Yelle, R. V., Jain, S. K., Cui, J., Montmessin, F., Schneider, N. M., et al. (2019). Detection of mesospheric CO_2 ice clouds on Mars in southern summer. *Geophysical Research Letters*, *46*(14), 7962–7971. https://doi.org/10.1029/2019GL082029

Kleinböhl, A., John Wilson, R., Kass, D., Schofield, J. T., & McCleese, D. J. (2013). The semidiurnal tide in the middle atmosphere of Mars. *Geophysical Research Letters*, *40*(10), 1952–1959. https://doi.org/10.1002/grl.50497

Korablev, O., Montmessin, F., Trokhimovskiy, A., Fedorova, A. A., Shakun, A. V., Grigoriev, A. V., et al. (2018). The Atmospheric Chemistry Suite (ACS) of three spectrometers for the ExoMars 2016 trace gas orbiter. *Space Science Reviews*, *214*(1), 7. https://doi.org/10.1007/s11214-017-0437-6

Lee, C., Lawson, W. G., Richardson, M. I., Heavens, N. G., Kleinböhl, A., Banfield, D., et al. (2009). Thermal tides in the Martian middle atmosphere as seen by the Mars climate sounder. *Journal of Geophysical Research*, *114*(3), E03005. https://doi.org/10.1029/2008JE003285

McCleese, D. J., Heavens, N. G., Schofield, J. T., Abdou, W. A., Bandfield, J. L., Calcutt, S. B., et al. (2010). Structure and dynamics of the Martian lower and middle atmosphere as observed by the Mars Climate Sounder: Seasonal variations in zonal mean temperature, dust, and water ice aerosols. *Journal of Geophysical Research*, *115*(12), 1–16. https://doi.org/10.1029/2010JE003677

McClintock, W. E., Schneider, N. M., Holsclaw, G. M., Clarke, J. T., Hoskins, A. C., Stewart, I., et al. (2014). The imaging ultraviolet spectrograph (IUVS) for the MAVEN mission. *Space Science Reviews*, *195*(1–4), 1–50. https://doi.org/10.1007/s11214-014-0098-7

McDunn, T. L., Bougher, S. W., Murphy, J., Smith, M. D., Forget, F., Bertaux, J. L., & Montmessin, F. (2010). Simulating the density and thermal structure of the middle atmosphere (∼80–130 km) of Mars using the MGCM-MTGCM: A comparison with MEX/SPICAM observations. *Icarus*, *206*(1), 5–17. https://doi.org/10.1016/j.icarus.2009.06.034

Millour, E., Forget, F., Spiga, A., Vals, M., Zakharov, V., Montabone, L., et al. (2018). The Mars climate database (version 5.3). In *Scientific workshop: "From Mars Express to ExoMars"*. ESAC. Retrieved from https://www.cosmos.esa.int/documents/1499429/1583871/Millour_E.pdf

Montmessin, F., Bertaux, J. L., Quémerais, E., Korablev, O., Rannou, P., Forget, F., et al. (2006). Subvisible CO_2 ice clouds detected in the mesosphere of Mars. *Icarus*, *183*(2), 403–410. https://doi.org/10.1016/j.icarus.2006.03.015

Montmessin, F., Korablev, O., Lefèvre, F., Bertaux, J. L., Fedorova, A., Trokhimovskiy, A., et al. (2017). SPICAM on Mars Express: A 10 year in-depth survey of the Martian atmosphere. *Icarus*, *297*, 195–216. https://doi.org/10.1016/j.icarus.2017.06.022

Nakagawa, H., Jain, S. K., Schneider, N. M., Montmessin, F., Yelle, R. V., Jiang, F., et al. (2020). A warm layer in the nightside mesosphere of Mars. *Geophysical Research Letters*, *47*(4), 1–10. https://doi.org/10.1029/2019GL085646

Nakagawa, H., Terada, N., Jain, S. K., Schneider, N. M., Montmessin, F., Yelle, R. V., et al. (2020). Vertical propagation of wave perturbations in the middle atmosphere on Mars by MAVEN/IUVS. *Journal of Geophysical Research: Planets*, *125*(9), 1–14. https://doi.org/10.1029/2020JE006481

Quémerais, E., Bertaux, J. L., Korablev, O., Dimarellis, E., Cot, C., Sandel, B. R., & Fussen, D. (2006). Stellar occultations observed by SPICAM on Mars Express. *Journal of Geophysical Research*, *111*(9), 1–12. https://doi.org/10.1029/2005JE002604

Schneider, N. (2022). MAVEN IUVS calibrated-level data product bundle. *NASA Planetary Data System*. https://doi.org/10.17189/1518946

Seiff, A., & Kirk, D. B. (1977). Structure of the atmosphere of Mars in summer at mid-latitudes. *Journal of Geophysical Research*, *82*(28), 4364–4378. https://doi.org/10.1029/js082i028p04364

Siddle, A. G., Mueller-Wodarg, I. C. F., Bruinsma, S., & Marty, J. C. (2021). Density structures in the Martian lower thermosphere as inferred by Trace Gas Orbiter accelerometer measurements. *Icarus*, *357*(February 2020), 114109. https://doi.org/10.1016/j.icarus.2020.114109

Smith, A. K. (2004a). Physics and chemistry of the mesopause region. *Journal of Atmospheric and Solar-Terrestrial Physics*, *66*(10), 839–857. https://doi.org/10.1016/j.jastp.2004.01.032

Smith, M. D. (2004b). Interannual variability in TES atmospheric observations of Mars during 1999–2003. *Icarus*, *167*(1), 148–165. https://doi.org/10.1016/j.icarus.2003.09.010

Smith, M. D. (2009). THEMIS observations of Mars aerosol optical depth from 2002-2008. *Icarus*, *202*(2), 444–452. https://doi.org/10.1016/j.icarus.2009.03.027

Smith, M. D., Bougher, S. W., Encrenaz, T., Forget, F., & Kleinböhl, A. (2017). Thermal structure and composition. Chapter 4 in *The atmosphere and climate of Mars* (pp. 42–75). Cambridge University Press. https://doi.org/10.1017/9781139060172

Starichenko, E. D., Belyaev, D. A., Medvedev, A. S., Fedorova, A. A., Korablev, O. I., Trokhimovskiy, A., et al. (2021). Gravity wave activity in the Martian atmosphere at altitudes 20–160 km from ACS/TGO occultation measurements. *Journal of Geophysical Research: Planets*, *126*(8), 1–15. https://doi.org/10.1029/2021JE006899

States, R. J., & Gardner, C. S. (1998). Influence of the diurnal tide and thermospheric heat sources on the formation of mesospheric temperature inversion layers. *Geophyiscal Research Letters*, *25*(9), 1483–1486. https://doi.org/10.1007/978-90-481-2642-2_304

States, R. J., & Gardner, C. S. (2000). Thermal structure of the mesopause region (80–105 km) at 40°N latitude. Part I: Seasonal variations. *Journal of the Atmospheric Sciences*, *57*(1), 66–77. https://doi.org/10.1175/1520-0469(2000)057<0066:TSOTMR>2.0.CO;2

Stone, S. W., Yelle, R. V., Benna, M., Elrod, M. K., & Mahaffy, P. R. (2018). Thermal structure of the Martian upper atmosphere from MAVEN NGIMS. *Journal of Geophysical Research: Planets*, *123*(11), 2842–2867. https://doi.org/10.1029/2018JE005559

Thiemann, E. M. B., Eparvier, F. G., Bougher, S. W., Dominique, M., Andersson, L., Girazian, Z., et al. (2018). Mars thermospheric variability revealed by MAVEN EUVM solar occultations: Structure at aphelion and perihelion and response to EUV forcing. *Journal of Geophysical Research: Planets*, *123*(9), 2248–2269. https://doi.org/10.1029/2018JE005550

Vandaele, A. C., Lopez-Moreno, J. J., Patel, M. R., Bellucci, G., Daerden, F., Ristic, B., et al. (2018). NOMAD, an integrated suite of three spectrometers for the ExoMars Trace gas mission: Technical description, science objectives and expected performance. *Space Science Reviews*, *214*(5), 80. https://doi.org/10.1007/s11214-018-0517-2

West, R., Crisp, D., & Chen, L. (1990). Mapping transformations for broadband atmospheric radiation calculations. *Journal of Quantitative Spectroscopy and Radiative Transfer*, *43*(3), 191–199. https://doi.org/10.1016/0022-4073(90)90051-7

Withers, P., Lorenz, R. D., & Neumann, G. A. (2002). Comparison of Viking lander descent data and MOLA topography reveals kilometer-scale offset in Mars atmosphere profiles. *Icarus*, *159*(1), 259–261. https://doi.org/10.1006/icar.2002.6914

Withers, P., Pratt, R., Bertaux, J. L., & Montmessin, F. (2011). Observations of thermal tides in the middle atmosphere of Mars by the SPICAM instrument. *Journal of Geophysical Research*, *116*(11), 1–17. https://doi.org/10.1029/2011JE003847

Yelle, R. V., Lunine, J. I., & Hunten, D. M. (1991). Energy balance and plume dynamics in Triton's lower atmosphere. *Icarus*, *89*(2), 347–358. https://doi.org/10.1016/0019-1035(91)90182-S

Yelle, R. V., Mahieux, A., Morrison, S., Vuitton, V., & Hörst, S. M. (2014). Perturbation of the Mars atmosphere by the near-collision with Comet C/2013 A1 (Siding Spring). *Icarus*, *237*, 202–210. https://doi.org/10.1016/j.icarus.2014.03.030

Zurek, R. W. (1976). Diurnal tide in the Martian atmosphere. *Journal of the Atmospheric Sciences*, *33*(2), 321–337. https://doi.org/10.1175/1520-0469(1976)033<0321:DTITMA>2.0.CO;2

Zurek, R. W., Tolson, R. H., Baird, D., Johnson, M. Z., & Bougher, S. W. (2014). Application of MAVEN accelerometer and attitude control data to Mars atmospheric characterization. *Space Science Reviews*, *195*(1–4), 303–317. https://doi.org/10.1007/s11214-014-0095-x